Y. Ito, A. Tsunoda, Y. Kurishita, S. Kitano, T. Nagasaki, “Experimental Visualization of Cryogenic Backflow Vortex Cavitation with Thermodynamic Effects”, Journal of Propulsion and Power, 32, pp.71–82 (Jan 2016)(The American Institute of Aeronautics and Astronautics: AIAA)

Experimental Visualization of Cryogenic Backflow Vortex Cavitation with Thermodynamic Effects

Yu Ito,* Atsuhiro Tsunoda,† Yuto Kurishita,‡ Satoshi Kitano,§ and Takao Nagasaki¶
Tokyo Institute of Technology, Yokohama 226-8502, Japan

The world's first test facility that allows the visualization of cavitation on a rotating inducer in both cryogen and water was used for comparing the cavitation features in liquid nitrogen at 77.9 K and water at 292.5 and 333.5 K. The test inducer was a triple-threaded helical one with a diameter of 65.3 mm and a rotational speed range of 3500–6000 rpm. The backflow vortex cavitation on the rotating inducer was quantitatively measured in the considered fluids. From the results, it was inferred that the backflow vortex cavitation orbital rate and its orbital diameter around the inducer axis depend on the head coefficient but are almost independent of the cavitation number and kind of fluid. Furthermore, the diameter of each backflow vortex cavitation column depends on the head coefficient, cavitation number, and kind of fluid. At the same head coefficient and cavitation number, the diameter in liquid nitrogen is 2.4 times smaller than that in water because of the thermodynamic effects. Moreover, the appearance of the cavitation is "foggy" in nitrogen and "foamy" in water. This difference can be explained by the maximum stable size of cavitation bubbles derived from the critical Weber number theory. Based on this theory, each cavitation bubble at the tip vortex regions in nitrogen is four times smaller than that in water.

Nomenclature

D	=	bubble diameter
d	=	orbital rotational diameter around inducer axis
P, P_{tot}	=	static pressure and total pressure
Q	=	volumetric flow rate
R	=	radius of inducer blade
S	=	area of usable flowpath normal to axis
s	=	surface tension
U	=	absolute fluid velocity
V	=	fluid velocity in axial direction
W	=	fluid velocity in rotational direction
We	=	Weber number, i.e., ratio of inertia of flow to surface tension
δ	=	diameter of each backflow vortex cavitation column
ζ	=	relative flow angle from a surface normal to axis in the rotational blade-fixed coordinate
ξ	=	blade helix angle from a surface normal to axis
ρ	=	density
σ	=	cavitation number
ϕ	=	flow coefficient
ψ	=	head coefficient
ω	=	rotational angular speed around inducer axis

Subscripts

bub	=	average cavitation bubble
c	=	critical value
hub	=	value at inducer blade hub
in	=	inlet
L	=	liquid phase
max	=	maximum
tip	=	value at inducer blade tip
V	=	saturation vapor phase

I. Introduction

CAVITATION has been one of the most difficult problems to overcome in the development of turbopumps for liquid-fueled rocket engines. As the cavitation number σ decreases, cavitation breakdown occurs. The cavitation number is given by

$$\sigma = \frac{P_{\text{in}} - P_V}{(1/2)\rho_L U_{\text{in}}^2} \tag{1}$$

where P_{in} is the fluid static pressure at the inlet, and P_V is the saturation vapor pressure corresponding to the fluid temperature at the inlet. Instead of σ, the net positive suction head (NPSH), $P_{\text{tot,in}} - P_V$, is often used because it is convenient to define $P_{\text{tot,in}}$ in terms of the tank pressure. High-performance engines require high combustion pressures for achieving large thrust and high specific impulse (ISP). Therefore, their turbopumps have to steadily discharge propellant at sufficiently high pressures to the combustor. In addition, turbopumps for rocket engines have to be compact, light, and operate at high rotational speeds. They also have to steadily suction the propellant at as low a pressure as possible, because lower tank pressures allow for thinner tank walls, making the rocket lighter and capable of carrying more payload. Consequently, cavitation is inevitable in space rocket turbopumps, and the combination of an inducer and a centrifugal pump is the best choice in this case. The inducer is generally a multithreaded helical axial pump, which has a low-pressure ratio and resists cavitation better than the centrifugal pump. On the other hand, the centrifugal pump is compact and has a high-pressure ratio, but the pump head abruptly fails if cavitation occurs. In the rocket turbopumps, the inducer first compresses the propellant and prevents cavitation from occurring in the centrifugal pump, which then boosts the pressure in one shot.

However, the performance of the inducer is affected by too much cavitation. As σ or the NPSH decreases, the inducer pump head remains the same as in cases of no cavitation. Furthermore, the maximum pump head can be achieved when cavitation stably occurs at a little higher σ or NPSH than at the cavitation breakdown. Finally, the inducer pump head abruptly fails at very low σ or NPSH. To use

*Assistant Professor, Department of Energy Sciences, 4259-G3-33-402 Nagatsuta-cho, Midori-ku, Kanagawa; itoyu110@00.alumni.u-tokyo.ac.jp. Senior Member AIAA.
†Graduate Student, Department of Energy Sciences; currently Engineer, Japan Aerospace Exploration Agency, Tanegashima, Kagoshima 891-3793, Japan. Member AIAA.
‡Graduate Student, Department of Energy Sciences; currently Engineer, Mitsubishi Heavy Industry, Ltd., Komaki, Aichi 485-8561, Japan.
§Undergraduate Student; currently Ph.D. Candidate, Department of Mechanical and Aerospace Engineering.
¶Associate Professor, Department of Energy Sciences.

the high-performance region effectively, it is necessary to allow controllable cavitation to occur at the inducer. A considerable number of studies has been conducted to investigate this effect, but they have mainly focused on water cavitation [1–3].

High-performance rocket engines use cryogens as propellant. For example, liquid hydrogen and liquid oxygen are used in the United States's RS-25, RL-10, and RS-68; Japan's LE-7A/5B; and Europe's Vulcain 2, whereas kerosene and liquid oxygen are used in Russia's RD-171/180/191 and the U.S. commercial Merlin series. Cryogens have thermodynamic features, referred to as "thermodynamic effects," which, consequently, decrease σ or NPSH at cavitation inception and cavitation breakdown, as well as improve the pump head at low σ or NPSH compred with room-temperature water. These thermodynamic effects were discovered for hot water in 1956 by Stahl et al. [4], who proposed a thermal criterion B known as "Stepanoff's B factor." The thermodynamic effects were then confirmed by Salemann [5] for hydrocarbons in 1959 and, in 1961, Stepanoff [6] experimentally and theoretically determined the laws governing the thermal cavitation performance of pumps. In 1965, Spraker [7] developed a parameter for thermal cavitation that was slightly different from Stepanoff's B factor and compared it with the experimental results obtained by Salemann [5] and Stepanoff [6].

Meng [8] conducted experiments in 1968 on a helical inducer in liquid hydrogen and showed that the NPSH at cavitation breakdown decreases at higher temperatures. Ball et al. [9] in 1969 visualized cavitation around a rotating inducer in liquid hydrogen and confirmed that the inducer performance was enhanced in hydrogen and increased as the hydrogen temperature increased. Moreover, they verified that cavitation in hydrogen has significantly higher thermodynamic effects compared with water. In 1969, Ruggeri and Moore [10] theoretically developed a method for predicting pump cavitation performance using two experimental references and compared the predicted values with experimental results for a helical inducer and two centrifugal impellers. Franc et al. [11] in 2004 used Freon™ (R114, dichloro-1,2-tetrafluoro-1,1,2,2-ethane, which has as much thermodynamic effect as hydrogen) for flow visualization of cavitation around an inducer and compared the results with those for water. They reported that the Prandtl number of R114 was different from that of cryogens. As the Prandtl number is very important for evaluating the thermodynamic effects, an alternative fluid is useful for studying them. However, using only an alternative fluid is not sufficient for understanding cryogenic thermodynamic effects because it is impossible to match all the dimensionless numbers in this case.

Therefore, cavitation in cryogen may differ from cavitation in water or Freon. To precisely control cryogenic cavitation, a deep understanding of its behavior and its influence on pump performance is required. Thus, visualization experiments play a very important role in developing more efficient and more reliable cryogenic pumps. Nonetheless, there have only been three reports on flow visualization of a rotating cryogenic impeller so far. The first was by Ball et al. at NASA [9] in 1969, the second was by Watanabe et al. at the Japan Aerospace Exploration Agency (JAXA) [12] in 2010, and the third was by the Kurishita et al. [13] and Ito et al. [14] at the Tokyo Institute of Technology in 2012. The experiments by NASA and JAXA used plastic as a transparent casing outside the inducer. Although plastic is easily workable, its linear expansion coefficient due to temperature change is higher than that of metal. In cryogens, the plastic casing shrinkage is several millimeters in diameter. Thus, a sufficiently large-diameter plastic casing at ambient temperature is required to achieve an adequate diameter when shrunk at the cryogenic temperature. This situation makes it difficult to keep the transparent casing axis aligned with the inducer axis during shrinking. Moreover, because the tip clearance affects cavitation, uniformity of tip clearance between the casing and the blade tip of the inducer is required. Janigro and Ferrini [15] pointed out in their lecture series at the von Kármán Institute for Fluid Dynamics in 1973 that the cavitation number at cavitation inception is affected by the tip clearance. Thus, additional mechanisms are required to keep the transparent casing axis aligned. Therefore, our test facility uses a quartz glass casing with a low coefficient of thermal expansion, which provides almost constant tip clearance in both cryogen and water. This allows for a test facility where accurate comparisons between cryogen and water can be conducted because the effects that depend on the facility, such as the resonance effect of piping and the effect of flow channel shapes, can be canceled.

Although many types of cavitation are observed at the inducer, this study focused on backflow vortex cavitation, which not only causes oscillating flows at the inducer but also affects the inducer performance. This is especially important because there are very few studies on the thermodynamic effects of backflow vortex cavitation. In 1958, Acosta [16] studied backflow vortex cavitation at the inducer inlet. Aoki and Yamamoto [17] observed backflow vortex cavitation using a laser Doppler velocimeter in 1992 and revealed its two major causes: one is the steep inverse pressure gradient at the tip clearance, and the other is the small axial flow momentum in this region. In 1997, Tsujimoto et al. [2] visualized backflow vortex cavitation using a high-speed video camera and reported that the orbital rotational rates of backflow vortex cavitation were less than the rotational rates of the inducer. Yokota et al. [18] in 1999 quantitatively measured the axial length, orbital rotational radius, and number of backflow vortex cavitation columns in water and organized these data by the flow coefficient. However, each data point was spread over a wide range for each flow coefficient. Recently, in 2015, Ehrlich and Murdock [19] compared cavitation on a rotating inducer in water at various temperatures in the range of 23.3–127°C (296.5–400.2 K). Backflow vortex cavitation was recorded in some of their photographs, but they did not investigate the phenomenon in detail.

In this study, a visualization facility was used for comparing cavitation at a rotating inducer in liquid nitrogen and in water. In addition, quantitative measurements were conducted, and the best way to organize these data was investigated. Furthermore, the thermodynamic effects of backflow vortex cavitation were also studied.

II. Experimental Setup

Ito et al. [20–22] have previously conducted visualization experiments and computational fluid dynamics simulations of cryogenic cavitation for convergent–divergent nozzle flow, flow around a thin hydrofoil, and flow through a cascade of plates. Therefore, the authors are familiar with some of the techniques for performing visualization experiments of cryogenic cavitation. Figure 1 shows the experimental facility used in this study for visualizing a rotating

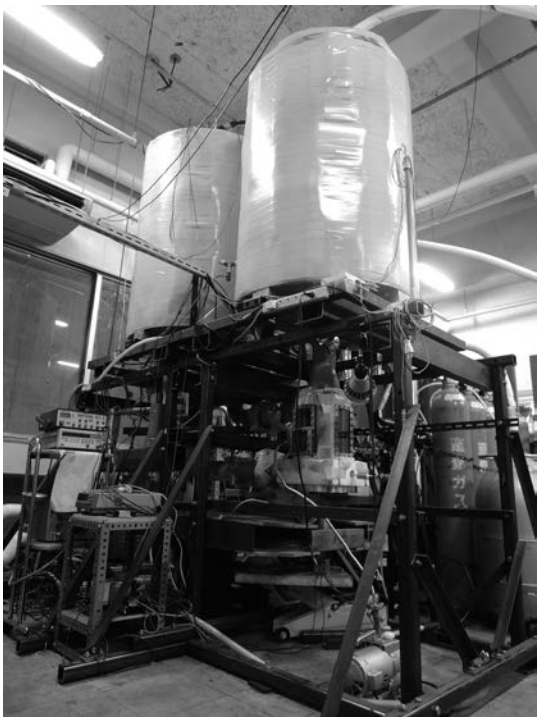

Fig. 1 Photograph of cavitation tunnel for visualization of cavitation on rotating inducer in both liquid nitrogen and water.

Inducer diameter : 65.30 mm
Hub diameter at leading edge : 20.18 mm
Hub diameter at trailing edge : 33.75 mm
Casing diameter : 66.30 mm
Tip clearance : 0.50 mm
Blade tip thickness : 1.25 mm
Number of blades : 3
Sweep back angle at leading edge : 50.00°
Center angle of blade helix arc : 318.45°
Blade helix angle at tip of leading edge : 10.00°
Blade helix angle at tip of trailing edge : 12.25°
Design flow coefficient : 0.10
Design head coefficient : 0.10

Fig. 2 Inducer specifications.

inducer with speeds of 0–8000 rpm. The transparent casing outside the inducer is made of quartz glass, so the tip clearance remains almost constant. All the other key parts were chosen based on their suitability for both cryogen and water at various temperatures. Therefore, this facility is the first in the world to allow the visualization of cavitation on a rotating inducer in both cryogen and water.

A. Test Inducer

Figure 2 shows the inducer used in this study as the test article. It was one of a series of NAL-TR696 inducers, which were triple-threaded helical inducers with a diameter of 65.3 mm designed by Kamijo et al. [23] at the National Aerospace Laboratory (NAL) of Japan (which is currently a part of JAXA) in 1982. The best of these inducers was used as the oxygen turbopump inducer in the second-stage engine LE-5 of Japan's launch rocket H-II. In 1985, Yamada et al. [24] performed nitrogen cavitation tests on another of these inducers at a design rate of 16,500 rpm. However, they carried out flow visualization only on a tube upstream of the inducer inlet, i.e., they did not visualize the flows around the inducer. In this study, we installed the test inducer in our visualization test facility as shown in Fig. 1.

The inducer was made of an Inconel™ superalloy with a linear expansion ratio of 12.6×10^{-6} 1/K. The transparent casing around the inducer was made of quartz glass, for which the liner expansion ratio was 2.7×10^{-6} 1/K at less than 273 K and 5.1×10^{-6} 1/K in the range of 273–373 K. Although these values are much less than 70.2×10^{-6} 1/K of the polycarbonate used by NASA and JAXA, thermal expansion should be considered. Table 1 shows the inducer diameters, casing inner diameters, and tip clearances at various temperatures used in experiments; and Fig. 3 illustrates the backflow vortex cavitation. The maximum value of the tip clearance was 0.56 mm in liquid nitrogen, and the minimum value was 0.49 mm in water at 330 K. The ratio of the tip clearance, $R_{\text{casing}} - R_{\text{tip}}$, to the blade width, $R_{\text{tip}} - R_{\text{hub}}$ [i.e., $(R_{\text{casing}} - R_{\text{tip}})/(R_{\text{tip}} - R_{\text{hub}})$] affects the backflow [15] and was 0.025 and 0.022 for liquid nitrogen and water, respectively. The results reflected this 0.003 error.

B. Cavitation Visualization Section

Figure 4 shows the structure of the inducer visualization section for the rotating inducer. Because of the clearance control in the test facility, flow visualization experiments were possible for both liquid nitrogen and water at various temperatures. To preserve the alignment of the casing with the inducer axis during thermal expansion, the casing was supported in the radial direction by two O rings suitable for both cryogen and water. Therefore, any change in the casing

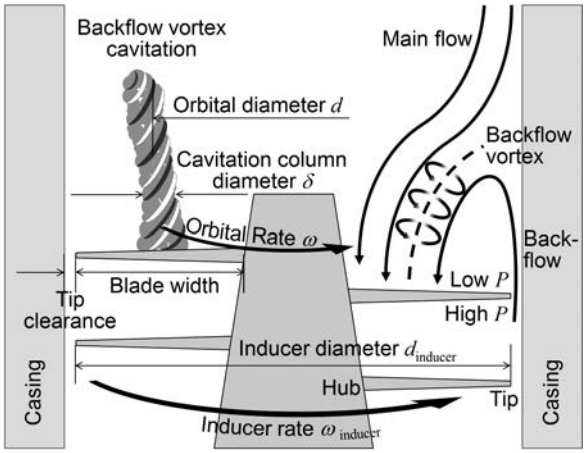

Fig. 3 Schematic of backflow vortex cavitation.

diameter due to thermal expansion was absorbed by the elasticity of the supporting O rings, and a uniform tip clearance was maintained around the inducer. As some of the pressure taps went through the casing, it was installed in a liquid-tight visualization pool. The casing and the feed line from the supply tank to the inducer were covered by fluid; therefore, they could be regarded as adiabatic walls. Each visualization window was double layered with an inner polycarbonate plate and an outer acrylic plate, and there was a vacuum layer in between to prevent frost.

The inducer was placed on top of a stainless shaft, which was supported by two bearings. In practical rocket engines and NAL's previous experiments, special bearings were used for cryogen. However, these do not work in water. Therefore, normal waterproof bearings were used in this study. When conducting liquid nitrogen experiments, it is especially important that the temperature of the upper bearing remains at room temperature. Therefore, thermostatic heaters were installed: one on the rotating shaft to heat the inner race of the upper bearing, and others on the flange near the outer race of the upper bearing. This arrangement worked well for the experiments in liquid nitrogen.

The inducer was driven by an inverter-controlled 3.7 kW ac motor with 6.25-fold stepup timing belts (the inducer rotated at 6000 rpm when the motor rotated at 960 rpm). The rotational rate of the inducer can be set within the range of 0–8000 rpm. In this study, it was controlled within 3500–6000 rpm and was measured by a rotational rate meter (Satotech DT-2230).

These devices allowed for accurate comparisons of the cavitation features in liquid nitrogen and water.

C. Tanks, Piping, and Thermal Insulator

Figure 4 shows a schematic of the test facility. There were two 600 L stainless tanks: one for supply, and the other for catch. These tanks were connected in parallel by three paths: one went through the inducer visualization section, another directly linked under the tanks, and the third linked the overhead tanks. The working fluid flowed from the supply tank through the inducer visualization section and a flow control valve to the catch tank. In addition, the fluid returned from the catch tank to the supply tank through the piping under the tanks. For each piping, there was a bellows to absorb the thermal stress. All the tanks, piping, and other components were thermally insulated with Dow Styrofoam and Insulpak no. 115.

Table 1 Tip clearance at different temperatures

Fluid	Temperature, K	Inducer diameter, mm	Casing diameter, mm	Hub diameter, mm	Inducer blade width, mm	Tip clearance, mm	Ratio of tip clearance to inducer blade width
Liquid nitrogen	78	65.14	66.27	20.13	22.50	0.56	0.025
— —	273.15	65.30	66.30	20.18	22.56	0.50	0.022
Water	290	65.31	66.31	20.18	22.56	0.50	0.022
Water	330	65.35	66.32	20.19	22.58	0.49	0.022

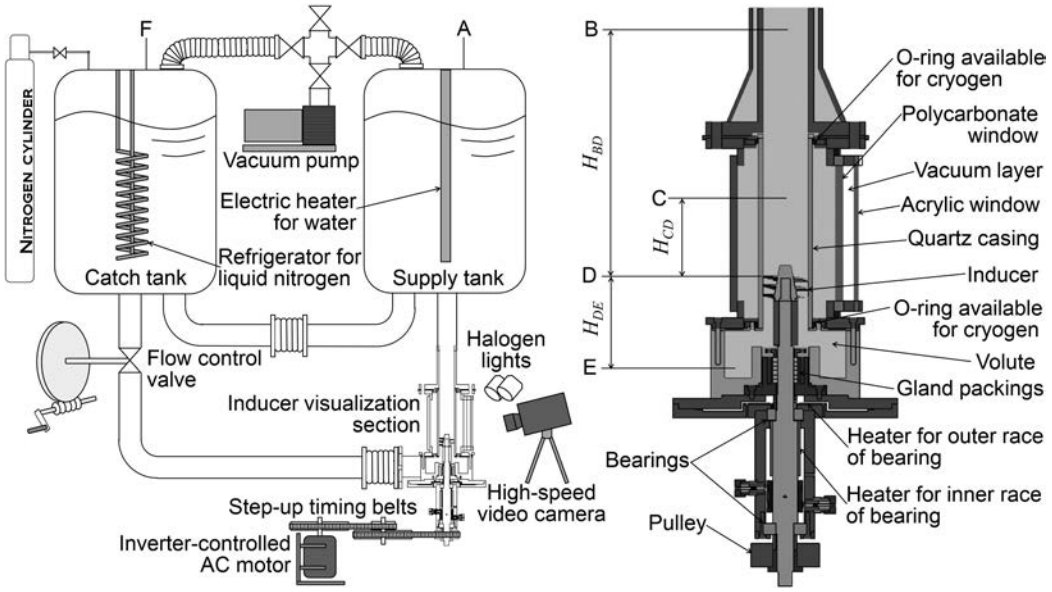

Fig. 4 Schematic of cavitation tunnel for visualization of cavitation on rotating inducer in both cryogen and water.

D. Observations and Measurements

A black-and-white high-speed video camera (Photron FASTCAM SA5), which had a recording rate of 12, 000 frames/s, a resolution of 896×704 pixels, and a digital shutter speed of $1/102,000$ s, was used with two 300 W halogen lights. It recorded at 120 frames per rotation of the inducer at the rotational rate of 6000 rpm.

To measure the pressure and temperature at point A to F in Fig. 4, eight electric pressure gauges and one thermocouple were installed as follows:

At points A and F, the pressures P_A and P_F in the two tanks were monitored by two electric pressure gauges (SUNX DP2-22Z). Furthermore, each tank had a differential pressure gauge to detect the fluid level so that the suitability of the tank levels, which were not visually observable, could be assessed.

At point B ($H_{BD} = 529$ mm in Fig. 4), there was a two-holed pitot tube for monitoring the inlet flow conditions. The total pressure $P_{\text{tot},B}$ and the static pressure P_B were measured by electric absolute pressure gauges (Kyowa PHS-10KA and Krone KDM30-200kPaA-A, respectively) with pressure accuracies of ± 2 kPa and ± 500 Pa, respectively. Moreover, the dynamic pressure $P_{\text{dyn},B}$ was directly measured by an electric differential pressure gauge (Validyne DP303-36-N-3-S-4-A), which had an accuracy of ± 175 Pa to precisely measure the small dynamic pressure.

At point C ($H_{CD} = 112$ mm), the inlet temperature was monitored by a T-type thermocouple. This thermocouple was compensated by saturated liquid nitrogen at 77.36 K for the experiments in liquid nitrogen and by iced water at 273.15 K for the experiments in water under atmospheric pressure.

Point D was the inlet of the test inducer.

At point E ($H_{DE} = 130$ mm), the total pressure $P_{\text{tot},E}$ was measured by an electric pressure gauge (Kyowa PHS-10KA) with an accuracy of ± 2 kPa.

A data-acquisition unit (Agilent 34970) was used to convert all the analog pressure and temperature data to digital signals, which were then transmitted to a PC. On the PC, a management software developed by the authors was run during the experiments. This software automatically received and processed the data to calculate the cavitation number, flow coefficient, and head coefficient; and the results were displayed on the PC. The detailed procedures for these calculations are presented in Sec. III. In addition, if the investigator had preliminarily input the target value for the flow coefficient, instructions on whether the flow control valve should be opened or closed in order to achieve the target flow coefficient were also displayed by the software.

The calibrations of all the pressure gauges, including analog-to-digital (A/D) conversion by Agilent 34970, were first conducted using a water column manometer as slope adjustments; the accuracy was ± 10 Pa when the pressure varied from the standard pressure. Furthermore, the calibration of the Krone KDM30-200kPaA-A was physically conducted using a barometer as a zero adjustment; the accuracy of P_B at atmospheric pressure was ± 50 Pa. The calibrations of all the other pressure gauges were then electrically conducted on the PC as zero adjustments using P_B as the standard pressure. In other words, when all the fluid was stationary in the test facility, electric calibrations were conducted as zero adjustments as follows:

$$P_{\text{tot},B} = P_B \tag{2}$$

$$P_{\text{dyn},B} = 0 \tag{3}$$

$$P_{\text{tot},E} = P_B + \rho_L g(H_{BD} + H_{DE}) \tag{4}$$

Moreover, the tip of the thermocouple was dipped in the compensating liquid nitrogen or water, and the calibration of the thermocouple, including A/D conversion, was conducted; the temperature accuracy was ± 0.05 K.

E. Flow Rate Control Valve

To control the flow rate, a flow control valve, which was a Fujikin 3-in.-diam ball valve made of stainless steel, was installed in the piping downstream of the inducer visualization section. In liquid nitrogen, it was very hard to precisely turn the valve to an arbitrary angle because the seal in the outer side of the ball was made of Teflon resin, which shrinks in liquid nitrogen. Therefore, we developed a worm-gear mechanism to precisely turn the valve even in liquid nitrogen.

F. Liquid Nitrogen Refrigerator and Electric Heater

In the liquid nitrogen experiments, a liquid nitrogen refrigerator developed by the authors was used to control the inlet cavitation number. It consisted of four evaporators, made of 12.6 m copper tubing with an outer diameter of 6 mm (deployed in parallel in the catch tank), and its refrigerating capability was approximately 2 kW at 78 K. In the refrigerator, the liquid nitrogen flowed and was

suctioned by a vacuum pump. Thus, the liquid nitrogen evaporated at a pressure lower than the saturation pressure corresponding to the liquid nitrogen temperature in the catch tank, which consequently decreased. On the other hand, in the water experiments, a 3.3 kW electric heater was used for controlling the inlet cavitation number.

In addition, nitrogen gas cylinders and a vacuum pump also played a role in controlling the inlet cavitation number.

III. Methodology

The working fluid (i.e., liquid nitrogen or water) flowed from the supply tank to the inducer visualization section, as shown in Fig. 4.

At point C, the inlet temperature T_C was measured. Because the flow channel was adiabatic from points B to D, the inducer inlet temperature $T_D = T_B = T_C$. Moreover, the fluid density ρ_L is a function of temperature but is almost independent of pressure; thus, $\rho_{L,B} = \rho_{L,C} = \rho_{L,D} = \rho_L(T_C)$. The accuracy of the density was ± 0.03 kg/m^3 in water and ± 0.23 kg/m^3 in liquid nitrogen.

At point B, the local axial velocity V_B and volumetric flow rate Q were calculated as

$$V_B = \sqrt{\frac{2P_{\mathrm{dyn},B}}{\rho_{L,B}}} \tag{5}$$

$$Q = S_B V_B \tag{6}$$

where S_B is the local area of the flowpath at point B normal to the axis.

At point D, the local area of the flowpath S_D was 3133 mm^2, which is different from the S_B value of 3452 mm^2 because there is a hub at the center of the inducer. Therefore, the local axial velocity V_D was

$$V_D = \frac{Q}{S_D} = \frac{S_B}{S_D} V_B \tag{7}$$

The accuracies of V_B and V_D were ± 0.01 m/s in water and ± 0.02 m/s in liquid nitrogen. The working fluid flowed into the inducer at a relative flow angle at the tip of the leading edge $\zeta_{\mathrm{tip},D}$ (i.e., a flow angle at the tip of the leading edge from a surface normal to its axis in the rotational-blade-fixed coordinate). Thus,

$$V_D = W_{\mathrm{tip}} \tan(\zeta_{\mathrm{tip},D}) = R_{\mathrm{tip}} \omega_{\mathrm{inducer}} \tan(\zeta_{\mathrm{tip},D}) \tag{8}$$

where W_{tip} is the rotational velocity at the blade tip, R_{tip} is the radius of the inducer blade, and $\omega_{\mathrm{inducer}}$ is the rotational angular speed of the inducer. The accuracy of W_{tip} was ± 0.04 m/s.

The dimensionless flow rate was then expressed by the flow coefficient ϕ as

$$\phi = \frac{V_D}{W_{\mathrm{tip}}} = \frac{V_D}{R_{\mathrm{tip}} \omega_{\mathrm{inducer}}} = \tan(\zeta_{\mathrm{tip},D}) \tag{9}$$

The accuracy of ϕ was ± 0.002. The maximum value $\phi_{\max}$ was attained by ϕ when $\zeta_{\mathrm{tip},D}$ equaled the blade helix angle at the tip of the leading edge $\xi_{\mathrm{tip},D}$:

$$\phi_{\max} = \tan(\zeta_{\mathrm{tip},D,\max}) = \tan(\xi_{\mathrm{tip},D} = 10^\circ) = 0.176 \tag{10}$$

On the other hand, the head coefficients ψ were calculated as

$$\psi = \frac{P_{\mathrm{tot},E} - P_{\mathrm{tot},B} - g \int_{-H_{DE}}^{H_{BD}} (\rho_L \mathrm{d}h)}{\rho_{L,D} W_{\mathrm{tip}}^2} = \frac{P_{\mathrm{tot},E} - P_{\mathrm{tot},B} - \rho_{L,B} g (H_{BD} + H_{DE})}{\rho_{L,B} R_{\mathrm{tip}}^2 \omega_{\mathrm{inducer}}^2} \tag{11}$$

because the head pressure due to gravity should be eliminated for evaluating the pump head. The accuracy of ψ was ± 0.01.

Moreover, the cavitation number σ was determined as

$$\sigma = \frac{P_D - P_{V,D}}{(1/2)\rho_{L,D} U_D^2} = \frac{\{P_B + g \int_0^{H_{BD}} (\rho_L \mathrm{d}h)\} - P_{V,D}}{(1/2)\rho_{L,D}[V_D^2 + W_{\mathrm{tip}}^2]} = \frac{(P_B + \rho_{L,B} g H_{BD}) - P_{V,B}}{(1/2)\rho_{L,B}[V_D^2 + W_{\mathrm{tip}}^2]} \approx \frac{P_B - P_{V,B} + \rho_L g H_{BD}}{(1/2)\rho_{L,B} R_{\mathrm{tip}}^2 \omega_{\mathrm{inducer}}^2} \tag{12}$$

where U_D is the inlet velocity at the inducer inlet, and $P_{V,D}$ is the saturation pressure corresponding to the temperature at the inducer inlet T_D. The accuracy of P_V was ± 60 Pa, so the accuracy of σ was ± 0.006.

In the present experiments, the Agilent 34970 unit that was used for converting the analog pressure and temperature data to digital signals was too slow to maintain the temperature measurement accuracy. Therefore, we did not measure the transient processes but instead waited for the flow coefficient to become steady. To achieve this, we altered the flow rate control valve so that the flow coefficient and head coefficient changed. Then, the fluid levels in the catch and supply tanks also changed, thus affecting the cavitation number, which in turn modified the flow coefficient again. After a certain period of time, all of these experimental conditions achieved steady values, even though backflow vortex cavitation is a periodic phenomenon, and we then recorded the data.

IV. Experimental Results and Discussion

A. Features of Backflow Vortex Cavitation

Figure 5 shows the cavitation pattern map in the field of the dimensionless flow coefficient $\phi/\phi_{\max}$ versus the cavitation number σ from Eq. (12). Here, the flow coefficient ϕ in Eq. (9) was reduced by the maximum flow coefficient $\phi_{\max}$ in Eq. (10). The inducer has no shroud, so a backflow (i.e., a flow in the adverse direction against the main flow as shown in Fig. 3) occurs from the pressure side to the suction side through the clearance between the blade tips and the outer casing. Then, a shear flow between the backflow and the blade tip creates a tip vortex at the tip near the leading edge. The tip vortex grows: first from the tip along the casing, and then toward the hub along the main flow on the surface of the inducer. The core of the tip vortex is at a lower pressure than the surroundings; therefore, cavitation occurs along the tip vortex, called "tip vortex cavitation." The photograph on the top right in Fig. 5 shows a typical tip vortex cavitation. As expressed in Eqs. (9) and (10), as ϕ approaches $\phi_{\max}$, the flow moves closer to the blade at the leading edge; thus, only a little cavitation occurs from the leading edge. On the other hand, the angle of the tip vortex cavitation from the blade increases as ϕ decreases, because the angle of the main flow from the blade increases as ϕ decreases. In addition, ψ increases as ϕ decreases according to a fundamental feature of axial pumps, causing more backflow to occur as ϕ decreases. These two factors make the tip vortex angle larger as ϕ decreases, which is confirmed by a comparison of the three photographs in the rightmost column of Fig. 5.

As σ decreases, cavitation occurs more easily in the low-pressure regions. Therefore, cavitation occurs from all the tip regions, as shown in the photographs in the leftmost column of Fig. 5, and the tip vortex cavitation becomes thick. Furthermore, a tornadolike vertical vortex cavitation, called "backflow vortex cavitation," is generated on the inducer surface. This can be easily distinguished in the leftmost two photographs in the bottom and middle rows of Fig. 5. The backflow vortex cavitation rotates around itself and moves orbitally around the inducer axis in the same rotational direction as the inducer. The orbital rotational rate of the backflow vortex cavitation is much slower than the rotational rate of the inducer; thus, the inducer blade overtakes the backflow vortex cavitation. The pressure is lower at the back of the rotating inducer blade and higher at the front of the blade. In some conditions, backflow vortex cavitation is observed at the back of the blade but not at the front. This means that a backflow vortex always exists on the inducer surface, regardless of whether cavitation exists or not. However, backflow vortex cavitation appears in the low-pressure region behind the blades but disappears in the high-pressure region in front of the blade.

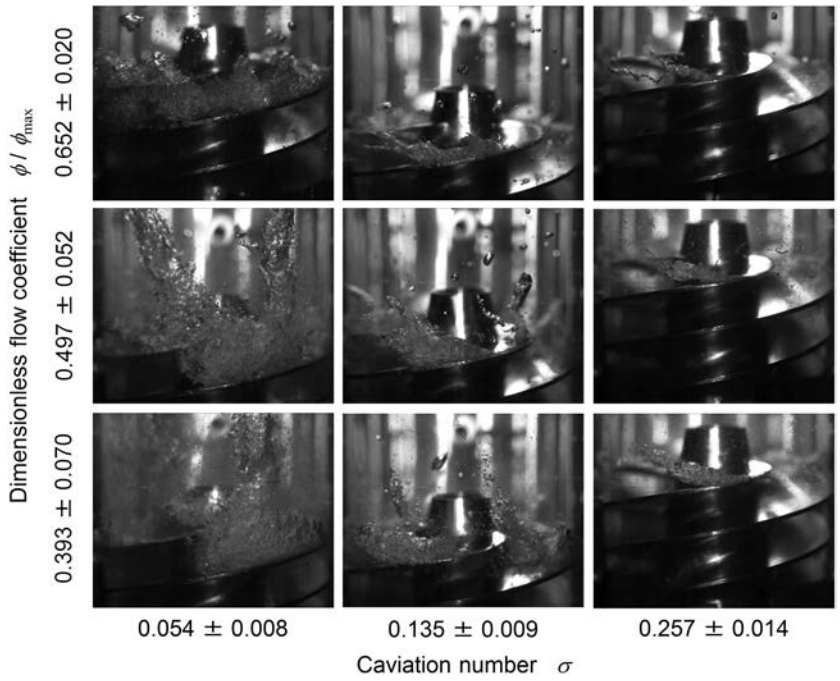

Fig. 5 Cavitation pattern map in field of flow coefficient versus cavitation number (water at 333.5 ± 4.0 K).

The backflow contains a rotational velocity component, which is affected by the rotating inducer. On the other hand, the main flow has little rotational velocity. Figure 3 shows a schematic of the mechanism of backflow vortex cavitation. The backflow makes a deep inroad into the main flow and is pushed back to the inducer surface by the main flow. At a contact surface between the backflow and the main flow, a shear flow is formed, and a backflow vortex is generated. Therefore, the backflow vortex rotates around itself in the same rotational direction as the inducer, because the outer flow of the backflow vortex is closer to the inducer rotational speed and the inner flow is closer to the main flow. In addition, the orbital rotation around the inducer axis also has the same direction as the inducer. As ϕ decreases, the reattaching position of the backflow vortex on the inducer blades (i.e., the position of the backflow vortex cavitation) moves toward the inducer hub because the backflow strengthens.

At small ϕ and σ, volumes of tip vortex cavitation, cavitation from all the tip regions, and backflow vortex cavitation increase.

B. Cavitation Difference Between Liquid Nitrogen and Water

In preliminary experiments, we compared the backflow vortex cavitation in water at 292.5 ± 1.3 K with that in water at 333.5 ± 4.0 K under almost the same cavitation number, flow coefficient, and head coefficient. We did not observe any significant differences between these two cases. In general, the thermodynamic effects in a certain fluid increase as the temperature increases. If much higher temperatures had been chosen, some differences would have been detected, as many researchers have reported [4–6,8,9,19]. In this study, the liquid nitrogen results at 77.9 ± 0.5 K, which are considered representative of cryogens with high thermodynamic effects, were compared with the water results at 333.5 ± 4.0 K, which are considered representative of fluids with low thermodynamic effects. The reason why we chose 333.5 ± 4.0 K water is that handling 333.5 ± 4.0 K water is easier than handling 292.5 ± 1.3 K water in order to control the cavitation number. This is because the same cavitation number can be achieved for 333.5 ± 4.0 K water at a higher pressure closer to the ambient pressure than for 292.5 ± 1.3 K water.

Figure 6 compares the backflow vortex cavitation in nitrogen at 77.5 K and in water at 337 K. In particular, the experimental conditions were almost the same in Figs. 6a and 6b. The cavitation in nitrogen seems to contain finer bubbles or cavities compared with that in water. This is because, in these experiments, the high-speed video camera recorded the reflected light from the surfaces of the bubbles or cavities, and the intensity of the reflected light increases proportionally with the surface area of the bubbles or cavities, and not with their volume. Therefore, a bright and foggy image is obtained for finer bubbles or cavities, and a dark and dappled image is obtained for larger and more-random bubbles or cavities. Furthermore, each fluid flow produces a different type of backflow vortex cavitation. The water flow produces backflow vortex cavitation containing thicker and larger linearly coupled cavities with smaller curvatures and tip vortex cavitation containing larger tandemly arrayed bubbles. On the other hand, the liquid nitrogen flow produces backflow vortex cavitation containing thinner and minuter linearly coupled cavities with larger curvatures and tip vortex cavitation containing tinier tandemly arrayed bubbles.

Sarosdy and Acosta [25] noted in their study in 1961 that the cavitation behind a disk in water was "clear and well defined" and that, in Freon, it was "indistinct and frothy." Freon has strong thermodynamic effects similar to cryogen, so a nitrogen cavity would be similar to a Freon cavity. Moreover, Gadd and Grant [26] visualized cavitation behind a disk in water in 1965, and they reported that a very sharp edge created a "glassy clear" cavity, whereas a dull edge produced a "rough and striated frosted-glassy" cavity. Ball et al. [9] visualized cavitation around a rotating inducer in liquid hydrogen in 1967. Although they did not mention the appearance of the cavitation in their paper, "foggy" cavitation in hydrogen can be seen in their visualization photographs. Franc et al. [11] visualized cavitation around a rotating inducer in Freon (R114) in 2004. In their photographs, the sheet cavitation from the leading edge on the inducer surface is white. This probably means that the sheet cavitation is a cavity with a rough and striated surface or it consists of small bubbles, because rougher and more-curved surfaces are whiter, whereas smoother and more-planar surfaces are blacker in photographs using reflected light. Thus, the cavitation in Freon observed by Franc et al. exhibits the same feature as that in Freon observed by Sarosdy and Acosta [25]. In 2012, Yoshida et al. [27] compared the cavitation around a rotating inducer in liquid nitrogen observed by Watanabe et al. [12] in 2010 with that in water at the same cavitation number, rotational rate, and flow rate. They described the cavitation in nitrogen as "creamy" and that in water as "icy."

Nonetheless, referring to Fig. 6, it would be more appropriate to say that the cavitation is foggy in nitrogen and foamy in water. In nitrogen, as shown in Figs. 6a and 6b, very tiny bubbles exist with the

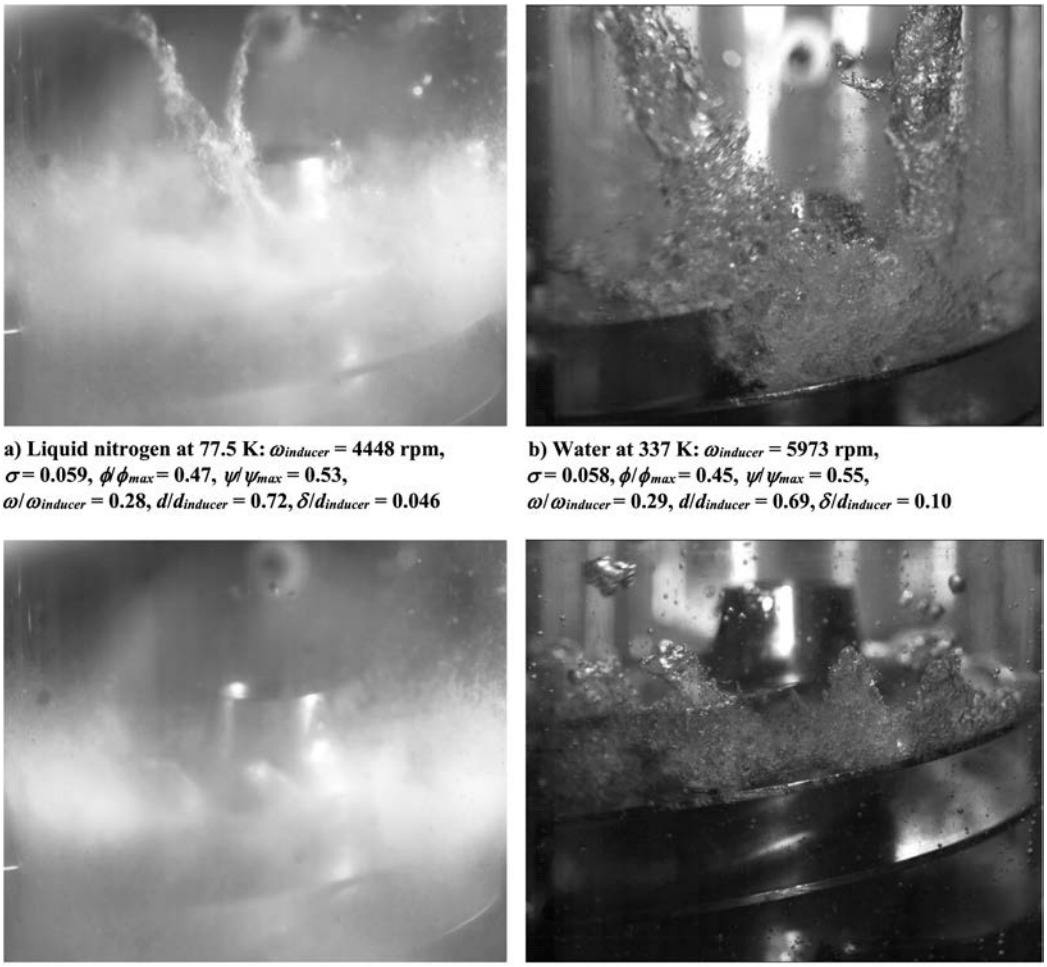

a) Liquid nitrogen at 77.5 K: $\omega_{inducer}$ = 4448 rpm, σ = 0.059, ϕ/ϕ_{max} = 0.47, ψ/ψ_{max} = 0.53, $\omega/\omega_{inducer}$ = 0.28, $d/d_{inducer}$ = 0.72, $\delta/d_{inducer}$ = 0.046

b) Water at 337 K: $\omega_{inducer}$ = 5973 rpm, σ = 0.058, ϕ/ϕ_{max} = 0.45, ψ/ψ_{max} = 0.55, $\omega/\omega_{inducer}$ = 0.29, $d/d_{inducer}$ = 0.69, $\delta/d_{inducer}$ = 0.10

c) Liquid nitrogen at 77.5 K: $\omega_{inducer}$ = 4448 rpm, σ = 0.071, ϕ/ϕ_{max} = 0.77, ψ/ψ_{max} = 0.34, $\omega/\omega_{inducer}$ = 0.22, $d/d_{inducer}$ = 0.90, $\delta/d_{inducer}$ = 0.036

d) Water at 337 K: $\omega_{inducer}$ = 5993 rpm, σ = 0.047, ϕ/ϕ_{max} = 0.63, ψ/ψ_{max} = 0.32, $\omega/\omega_{inducer}$ = 0.14, $d/d_{inducer}$ = 0.96, $\delta/d_{inducer}$ = 0.072

Fig. 6 Comparison of backflow vortex cavitation in liquid nitrogen and water.

fog in the backflow region around the blade tip. These bubbles are generated by shearing between the backflow and the blade tip and are transported to the tip vortex region. Thus, even the tip vortex cavitation consists of foggy bubbles. On the contrary, the backflow vortex cavitation is generated on site at the core of the backflow vortex and is therefore a continuum vapor cavity. However, as shown in Figs. 6a and 6b, it is apparently thinner and more separated than that in water. This is one of the reasons for the thermodynamic effects in cryogen, and its mechanism will be explained in Sec. IV.E.

On the other hand, in water, as shown in Figs. 6a and 6b, the outlines of the cavitation are very clear. Bubbles are generated by shearing between the backflow and the blade tip, and the size of these bubbles can be clearly explained using the Weber number We, which is the ratio of the inertia of a flow to the surface tension, based on the bubble breakup theory by Hinze [28]. Although his theory was originally proposed for droplets, other researchers have extended the theory to the breakup and coalescence of bubbles:

$$We = \frac{\rho_L U^2 D_{\text{bub}}}{s_L} \tag{13}$$

where D_{bub} is the average size of the cavitation bubbles, and s_L is the surface tension. If the kinds of fluid and temperature are known, the values of ρ_L and s_L can be fixed. At the tip vortex regions in Figs. 6a and 6b, U^2 is as follows:

$$U^2 = V^2 + W_{\text{tip}}^2 = \phi^2 W_{\text{tip}}^2 + W_{\text{tip}}^2 = (\phi^2 + 1) R_{\text{tip}}^2 \omega_{\text{inducer}}^2 \tag{14}$$

Azad and Syeda [29] stated that a critical Weber number We_c exists at a point where the cohesive and disruptive forces are balanced, resulting in a maximum stable size. Therefore, the maximum stable size $D_{\text{bub,max}}$ is expressed as follows:

$$D_{\text{bub,max}} = We_c \frac{s_L}{U^2 \rho_L} \tag{15}$$

Because We_c is a constant, $D_{\text{bub,max}}$ is proportional to $s_L/(U^2\rho_L)$. At the tip vortex regions in Figs. 6a and 6b, $s_L/(U^2\rho_L) = 1.09 \times 10^{-8}$ m in liquid nitrogen and $s_L/(U^2\rho_L) = 3.98 \times 10^{-8}$ m in water; thus, the nitrogen bubbles are four times smaller than the water bubbles. Furthermore, because the surface tension is larger in water, the water bubbles are stickier. Therefore, a foam of bubbles accumulates on the blade tips, and the tip vortex cavitation consists of foamy bubbles.

The relationship in Eq. (15) can be applied to cases of the same liquid at different temperatures, and some previous results provide evidence for this criterion. For example, Sarosdy and Acosta presented photographs of water cavitation formed on a small disk in Fig. 1 of [25] in 1961. The cavitation was a continuum cavity around the disk in water at 208°F (370.9 K) but consisted of foamy bubbles in water at 245°F (391.5 K). Uchiumi et al. included photographs of water cavitation formed on a rotating inducer in Fig. 11 of [30] in 2003. The water cavitation at room temperature in their experiment contained tinier bubbles compared with the water cavitation at 337 K in our experiments, shown in Figs. 6b and 6d. This is because the blade speed of their inducers, which had a diameter of 174 or 162 mm at 7500 rpm, was faster than that of our inducer, which has a diameter

of 65 mm at 6000 rpm. Therefore, their value of U in Eq. (15) was larger than our value. Recently, Ehrlich and Murdock reported cavitation on a rotating inducer in water at 23.3°C (296.5 K) in Fig. 6 of [19] in 2015. The water cavitation at 23.3°C contained bubbles with almost the same size as the water bubbles at 337 K in our experiments, as shown in Figs. 6b and 6d. This is because the blade speed of their inducers, which had a diameter of 75.77 mm at 3000–6000 rpm, was almost the same as that of our inducer, which has a diameter of 65.3 mm at 6000 rpm; thus, their U value in Eq. (15) was almost the same as our value.

As mentioned before, the backflow contains a rotational velocity component, which is affected by the rotating inducer, but the main flow has little rotational velocity, as shown in Fig. 3. Thus, the outer surface is faster than the inner one. In this condition, a Taylor vortex [31] is formed in the shear regions between the backflow and the main flow; and, as a result, the backflow vortex cavitation is not smooth. Based on Taylor's experiments and theory, the rotations where the outer surface is faster than the inner surface are stable. Therefore, the backflow vortex is always stable and remains so while it is being generated by shearing between the backflow and the main flow. In this case, the rotational rate around each backflow vortex is fastest at the tip where the backflow penetrates and decreases closer to the blade surface. This is because the rotational momentum remains constant throughout the backflow vortex, but the mass of the backflow vortex increases as a result of entrainment of the surrounding fluid. In fact, all of the backflow vortex cavitation twists in the same rotational direction as the inducer because it rotates faster around its center in the upper section than in the lower section.

Moreover, in Figs. 6c and 6d, several small backflow vortex cavitation columns are observed at almost the same head coefficient even though the cavitation number and flow coefficient are different. In this case, the number of backflow vortex cavitation columns and their heights are similar to each other. However, the appearance of the cavitation is quite different, being foggy in nitrogen and foamy in water.

C. Orbital Rotational Rate of Backflow Vortex Cavitation Around Inducer Axis

Figure 7a shows the relationship between the dimensionless orbital rotational rate $\omega/\omega_{\text{inducer}}$ of the backflow vortex cavitation around the inducer axis and $\phi/\phi_{\max}$. Here, the orbital rate around the inducer axis ω is reduced by the rotational rate ω_{inducer} of the inducer, as shown in Fig. 3. Yokota et al. [18] also sorted their data by the flow coefficient, but in their figure, the data were a little scattered. In Fig. 7a, there were few effects of the cavitation number and working fluid on $\omega/\omega_{\text{inducer}}$. At $\phi/\phi_{\max} = 0$, the main flow is stationary in the axial direction. Therefore, the flow around the inducer at $\phi/\phi_{\max} = 0$ rotates at the same rotational speed as the inducer with an axial speed of zero. Thus, $\omega/\omega_{\text{inducer}}$ achieves unity, and the correlation curve must go through $\omega/\omega_{\text{inducer}} = 1$ at $\phi/\phi_{\max} = 0$. The correlation is given by

$$\omega/\omega_{\text{inducer}} = \frac{0.135}{\phi/\phi_{\max} + 0.135} \tag{16}$$

From this correlation, $\omega/\omega_{\text{inducer}}$ has a nonzero value of 0.119 at $\phi/\phi_{\max} = 1$. This is because the backflow vortex is generated not only by the backflow through the clearance but also by the leading edge. It is known that there is a backflow vortex generated by the leading edge in a shrouded centrifugal impeller.

Figure 7b shows the relationship between $\omega/\omega_{\text{inducer}}$ and the dimensionless head coefficient $\psi/\psi_{\max}$, in which ψ in Eq. (11) is reduced by $\psi_{\max}$. In this inducer, $\psi_{\max} = 0.25$ at $\phi/\phi_{\max} = 0$ without cavitation. The data in Fig. 7b converge better than those in Fig. 7a, and the intensity of the backflow is proportional to the head coefficient but not the flow coefficient. In addition, when there is slight or no cavitation, the head coefficient is uniquely determined by the flow coefficient. Therefore, the backflow vortex cavitation can be sorted by the flow coefficient only in cases when the head coefficient does not drop because of cavitation. Thus, the backflow vortex cavitation could be sorted simply by the head coefficient. In Fig. 7b, there are also few effects of the cavitation number and working fluid on $\omega/\omega_{\text{inducer}}$. This implies that ω is decided by the fluid dynamics and is independent of thermodynamic properties. In this case, the correlation curve must go through $\omega/\omega_{\text{inducer}} = 0.119$ at $\psi/\psi_{\max} = 0$ from Eq. (16) because $\psi/\psi_{\max} = 0$ at $\phi/\phi_{\max} = 1$. The correlation is given by

$$\omega/\omega_{\text{inducer}} = 0.877[\psi/\psi_{\max}]^{2.63} + 0.119 \tag{17}$$

D. Orbital Rotational Diameter of Backflow Vortex Cavitation Around Inducer Axis

Figure 8a shows the relationship between the dimensionless orbital rotational diameter d/d_{inducer} of the backflow vortex cavitation around the inducer axis and $\phi/\phi_{\max}$, and Fig. 8b shows the relationship between d/d_{inducer} and $\psi/\psi_{\max}$. Here, the orbital diameter around the inducer axis d is reduced by the inducer diameter d_{inducer}, as shown in Fig. 3. The data in Fig. 8a are a little scattered, whereas those in Fig. 8b converge better. This is also because the intensity of the backflow is proportional to the head coefficient but not the flow coefficient. Therefore, the backflow vortex cavitation should be sorted by the head coefficient as well. In these figures, there are also few effects of the cavitation number and working fluid on d/d_{inducer}, implying that d is also decided by fluid dynamics and is independent of thermodynamic properties.

In Fig. 8b, at $\psi/\psi_{\max} = 0$, there is no backflow through the tip clearance, so the backflow vortex is generated only by the leading edge. Therefore, the correlation curve should go through $d/d_{\text{inducer}} = 1$ at $\psi/\psi_{\max} = 0$ and is given by

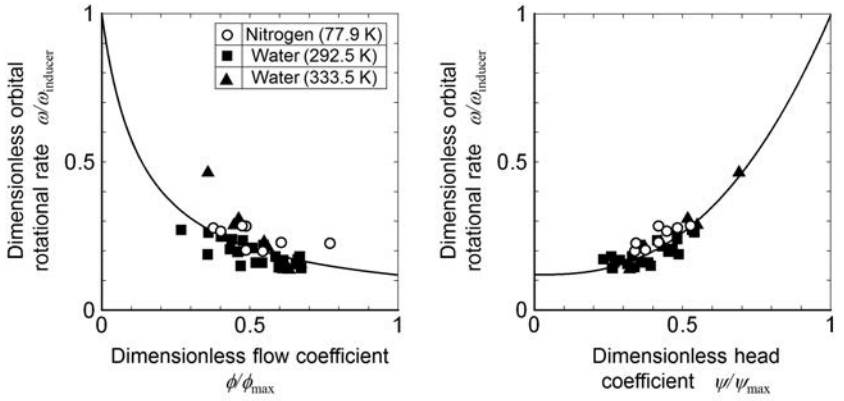

a) Orbital rotational rate vs flow coefficient b) Orbital rotational rate vs head coefficient

Fig. 7 Orbital rotational rate of backflow vortex cavitation.

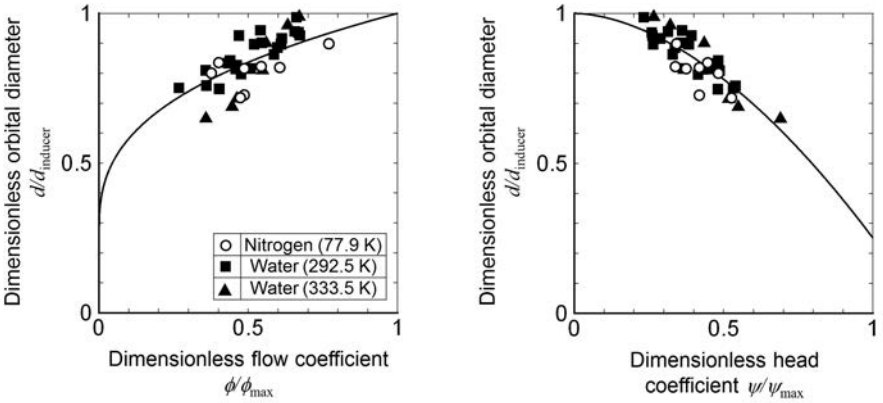

a) Orbital rotational diameter vs flow coefficient **b) Orbital rotational diameter vs head coefficient**

Fig. 8 Orbital rotational diameter of backflow vortex cavitation.

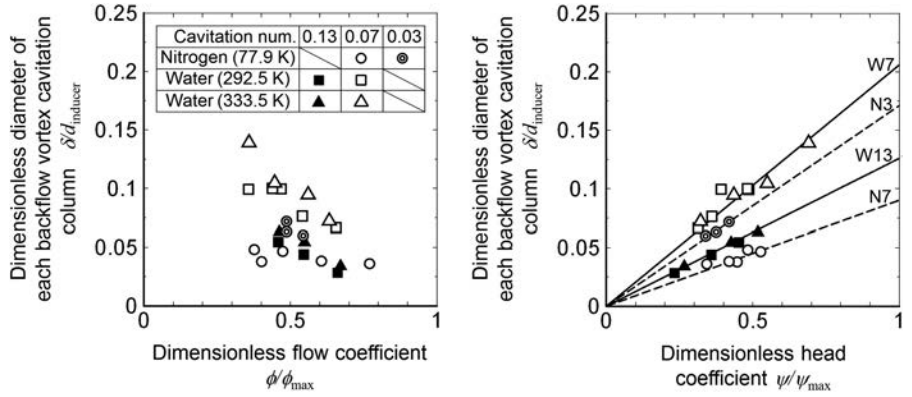

a) Diameter of each backflow vortex cavitation column vs flow coefficient **b) Diameter of each backflow vortex cavitation column vs head coefficient**

Fig. 9 Diameter of each backflow vortex cavitation column.

$$d/d_{\text{inducer}} = -0.749[\psi/\psi_{\max}]^{1.77} + 1 \tag{18}$$

From this equation, $d/d_{\text{inducer}} = 0.251$ at $\psi/\psi_{\max} = 1$.

On the other hand, in Fig. 8a, $\phi/\phi_{\max} = 0$ corresponds to $\psi/\psi_{\max} = 1$. Thus, the correlation curve should go through $d/d_{\text{inducer}} = 0.251$ at $\phi/\phi_{\max} = 0$ and is given by

$$d/d_{\text{inducer}} = 0.749[\phi/\phi_{\max}]^{0.355} + 0.251 \tag{19}$$

E. Diameter of Each Backflow Vortex Cavitation Column

Figure 9a shows the relationship between the dimensionless diameter of each backflow vortex cavitation column, $\delta/d_{\text{inducer}}$, and $\phi/\phi_{\max}$; and Fig. 9b shows the relationship between $\delta/d_{\text{inducer}}$ and $\psi/\psi_{\max}$. Here, the cavitation diameter of each backflow vortex cavitation column δ is reduced by d_{inducer}, as shown in Fig. 3. In Fig. 9, the cavitation number and working fluid affect $\delta/d_{\text{inducer}}$. In the experiments, the temperatures had accuracies of ± 0.5 K at 77.9 K, ± 1.3 K at 292.5 K, and ± 4.0 K at 333.5 K. Furthermore, the accuracies of the cavitation numbers were ± 0.01 at $\sigma = 0.03$, ± 0.02 at $\sigma = 0.07$, and ± 0.03 at $\sigma = 0.13$. The data for each cavitation number and working fluid in Fig. 9a are a little scattered, whereas the data in Fig. 9b converge better, implying that δ should also be sorted by the head coefficient.

In Fig. 9b, the results at $\sigma = 0.13$ in hot water (black triangles) and those at $\sigma = 0.13$ in cold water (black squares) have similar tendencies. Furthermore, the results at $\sigma = 0.07$ in hot water (white triangles) and those at $\sigma = 0.07$ in cold water (white squares) also have similar tendencies. In other words, there are no significant differences between the cold and hot water results, as mentioned in Sec. IV.B. However, the difference in the cavitation number affects $\delta/d_{\text{inducer}}$.

Figure 10 illustrates the mechanisms of each backflow vortex cavitation column diameter. First, let us compare the two figures at the top. At small cavitation numbers, the saturation pressure is relatively high. Thus, the region with pressure below the saturation pressure enlarges, and the diameter of each backflow vortex cavitation column increases. On the other hand, the saturation pressure is relatively low at large cavitation numbers. Thus, the region with pressure below the saturation pressure shrinks, and the diameter of each backflow vortex cavitation column decreases. In other words, the diameter of each backflow vortex cavitation column changes because of the cavitation number, even for the same intensity of the backflow vortex. Next, let us compare the two figures on the left. At low head coefficients, the backflow vortex rotates slower around itself. This slow rotation makes the vortex core pressure relatively high, and thus the diameter of each backflow vortex cavitation column decreases. On the other hand, at high head coefficients, the backflow vortex rotates faster around itself. This fast rotation makes the vortex core pressure much lower than the saturation pressure, and thus the diameter of each backflow vortex cavitation column increases.

In Fig. 9b, the results at $\sigma = 0.07$ in liquid nitrogen (white circles) are much smaller than those in hot and cold water (white squares and triangles). The correlation between lines N3 and N7 is

$$\delta/d_{\text{inducer}} = \frac{0.0104}{\sigma_{\text{nitrogen}}^{0.8}}[\psi/\psi_{\max}] \tag{20}$$

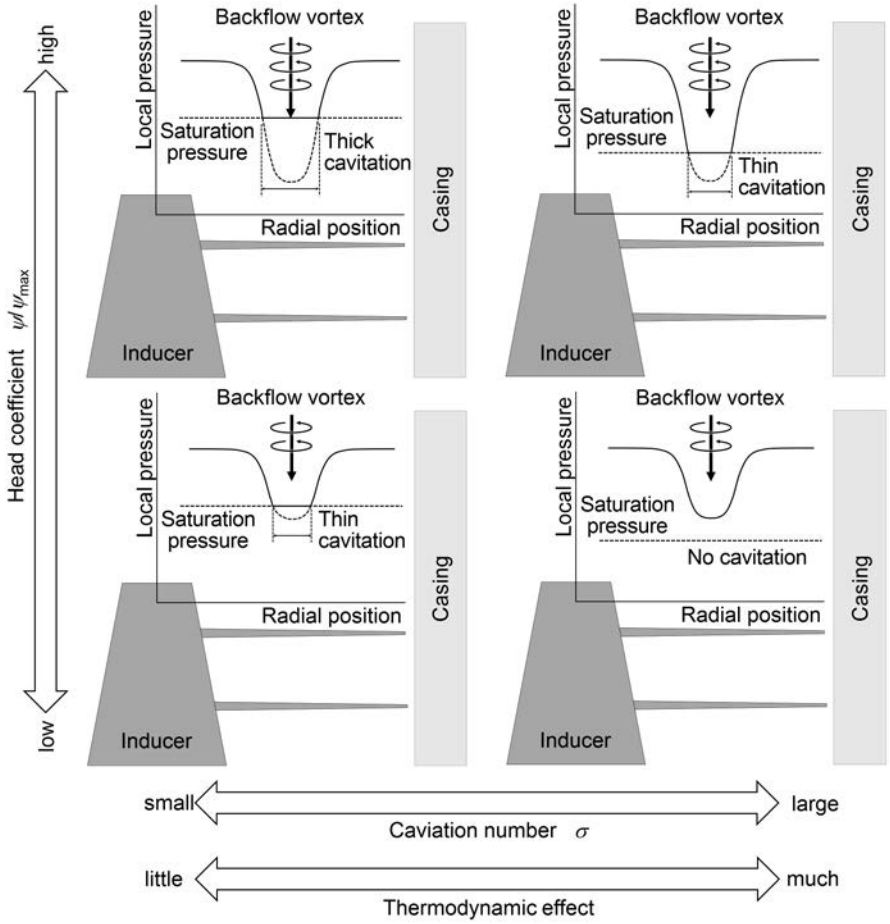

Fig. 10 Schematic of each backflow vortex cavitation column diameter.

and the correlation between lines W7 and W13 is

$$\delta/d_{\text{inducer}} = \frac{0.0245}{\sigma_{\text{water}}^{0.8}}[\psi/\psi_{\max}] \tag{21}$$

This is one of the consequences of the thermodynamic effects in liquid nitrogen, which implies that the liquid nitrogen temperature and saturation pressure reduce during evaporation. This corresponds to an increase in the cavitation number, so $\delta/d_{\text{inducer}}$ in liquid nitrogen is approximately 2.4 times smaller than those in hot and cold water. In Fig. 9b, the results at $\sigma = 0.03$ in liquid nitrogen (double circles) are also smaller than the results at $\sigma = 0.07$ in hot and cold water (white squares and triangles), even though the smaller σ causes a larger $\delta/d_{\text{inducer}}$.

V. Conclusions

The world's first test facility that allows the visualization of cavitation on a rotating inducer in both cryogen and water was developed, and it was used to compare the cavitation features in liquid nitrogen at 77.9 ± 0.5 K and water at 292.5 ± 1.3 K and 333.5 ± 4.0 K. The tested inducer was a triple-threaded helical one with a diameter of 65.3 mm and a speed range of 3500–6000 rpm. The tip clearance between the casing and the blade tip of the inducer was made almost constant for both liquid nitrogen and water by using quartz glass for the transparent casing and by installing the casing inside a liquid-tight visualization pool. Hence, the backflow vortex cavitation on the rotating inducer was observed in both liquid nitrogen and water, and the thermodynamic effects of backflow vortex cavitation were evaluated quantitatively.

From the results, the following conclusions were drawn:

1) The orbital rotational rate around the inducer axis of the backflow vortex cavitation was quantitatively measured. It was inferred that the data should be sorted by the head coefficient rather than the flow coefficient. As the head coefficient increases, the orbital rotational rate approaches the inducer rate. On the other hand, as the head coefficient tends to zero, the orbital rotational rate approaches a certain small value because the backflow vortex cavitation is generated not only by the backflow through the tip clearance but also by the leading edge of the inducer blade.

2) The orbital rotational diameter around the inducer axis of the backflow vortex cavitation was quantitatively measured. It was concluded that these data should be also sorted by the head coefficient rather than the flow coefficient. As the head coefficient increases, the orbital rotational diameter approaches the hub diameter of the inducer because the backflow strengths against the main flow. On the other hand, as the head coefficient tends to zero, the orbital rotational diameter approaches the diameter of the inducer because the backflow vortex cavitation is formed around the inducer tip.

3) The diameter of each backflow vortex cavitation column was quantitatively measured. It was deduced that these data should also be sorted by the head coefficient rather than the flow coefficient. In the same fluid at the same cavitation number, the diameter of each backflow vortex cavitation column is proportional to the head coefficient because, as each backflow vortex rotates faster, the cavitation region (i.e., the region at pressure below the saturation pressure) enlarges. Moreover, in the same fluid at the same head coefficient, as the cavitation number decreases, the diameter of each backflow vortex cavitation column increases because the saturation pressure increases relative to the pressure at the inducer inlet, and thus the region at pressure below the saturation pressure enlarges. Furthermore, under the same cavitation number and the same head coef-

ficient, the diameter of each backflow vortex cavitation column in liquid nitrogen is 2.4 times smaller than that in water because of the thermodynamic effects.

4) The appearance of the cavitation is foggy in nitrogen and foamy in water. The difference can be explained by the maximum stable size of the cavitation bubbles derived from the critical Weber number theory. Based on this theory, for example, the size of each cavitation bubble on the test inducer at the tip vortex regions in liquid nitrogen at 77.9 K is four times smaller than that in water at 333.5 K at the cavitation number of 0.059, the dimensionless flow coefficient of 0.47, and the dimensionless head coefficient of 0.53. Furthermore, this theory can explain the appearance of the cavitation observed not only by the authors but also by Sarosdy and Acosta in 1961 [25], Uchiumi et al. in 2003 [30], and Ehrlich and Murdock in 2015 [19]. In a future study, if the size of each cavitation bubble is quantitatively measured under various conditions, this theory could be validated, and the critical Weber number could be estimated.

Acknowledgments

This work was financially supported by the Iwatani Naoji Foundation and the Engineering Digital Innovation (JEDI) Center at the Japan Aerospace Exploration Agency. The authors thank Emeritus Toshio Nagashima, Susumu Teramoto, Koji Okamoto, and Kazuo Yamaguchi at the University of Tokyo, as well as Naoki Tani and Kazuki Niiyama at IHI Corporation, who provided the stainless tanks, inducer shaft, volute section, and their advice. Moreover, the authors thank the Precision and Manufacturing Center at the Tokyo Institute of Technology, which fabricated and adjusted the inducer section. In addition, the authors are grateful to Soshi Fukao at the Tokyo Institute of Technology, who took the photograph of the facility.

References

[1] Stripling, L. B., and Acosta, A. J., "Cavitation in Turbopumps – Part 1," *Journal of Basic Engineering*, Vol. 84, No. 3, 1986, pp. 326–338. doi:10.1115/1.3657314

[2] Tsujimoto, Y., Yoshida, Y., Maekawa, Y., Watanabe, S., and Hashimoto, T., "Observations of Oscillating Cavitation of an Inducer," *Journal of Fluids Engineering*, Vol. 119, No. 4, 1997, pp. 775–781. doi:10.1115/1.2819497

[3] Torre, L., Pasini, A., Cervone, A., Pace, G., Miloro, P., and D'Agostino, L. Y., "Effect of Tip Clearance on the Performance of a Three-Bladed Axial Inducer," *Journal of Propulsion and Power*, Vol. 27, No. 4, 2011, pp. 890–898. doi:10.2514/1.B34067

[4] Stahl, H. A., and Stepanoff, A. J., "Thermodynamic Aspects of Cavitation in Centrifugal Pumps," *Transactions of ASME*, Nov. 1956, pp. 1691–1693.

[5] Salemann, V., "Cavitation and NPSH Requirements of Various Liquids," *Journal of Basic Engineering*, Vol. 81, No. 2, 1959, pp. 167–180.

[6] Stepanoff, A. J., "Cavitation in Centrifugal Pumps with Liquids Other than Water," *Journal of Engineering for Power*, Vol. 83, No. 1, 1961, pp. 79–89. doi:10.1115/1.3673147

[7] Spraker, W. A., "The Effects of Fluid Properties on Cavitation in Centrifugal Pumps," *Journal of Engineering for Power*, Vol. 87, No. 3, 1965, pp. 309–318. doi:10.1115/1.3678264

[8] Meng, P. R., "Change in Inducer Net Positive Suction Head Requirement with Flow Coefficient in Low Temperature Hydrogen (27.9° to 36.6°R)," NASA TN-D-4423, 1968.

[9] Ball, C. L., Meng, P. R., and Reid, L., "Cavitation Performance of 84° Helical Inducer Operated in 37° and 42°R Liquid Hydrogen," NASA TM-X-1360, 1969.

[10] Ruggeri, R. S., and Moore, R. D., "Method for Prediction of Pump Cavitation Performance for Various Liquids, Liquid Temperatures, and Rotative Speeds," NASA TN-D-5292, 1969.

[11] Franc, J. P., Rebattet, C., and Coulon, A., "An Experimental Investigation of Thermal Effects in a Cavitating Inducer," *Journal of Fluids Engineering*, Vol. 126, No. 5, 2004, pp. 716–723. doi:10.1115/1.1792278

[12] Watanabe, M., Nagaura, K., Hasegawa, S., Niiyama, K., Yoshida, Y., and Sugita, E., "Direct Visualization for Cavitating Inducer in Cryogenic Flow (3rd Report: Visual Observations of Cavitation in Liquid Nitrogen)," Japan Aerospace Exploration Agency Rept. RM-09-010, Miyagi, Japan, 2010.

[13] Kurishita, Y., Ito, Y., and Nagasaki, T., "Test Facility for Cavitation Visualization of Turbo Pump Inducer in Liquid Nitrogen and Water," *Asian Joint Conference on Propulsion and Power* [CD-ROM], Chinese Soc. of Engineering Thermophysics (CSET) AJCPP2012-093, Beijing, 2012.

[14] Ito, Y., Kurishita, Y., Kitano, S., and Nagasaki, T., "New Visualization Test Facility for Liquid Nitrogen and Water Cavitation in Rotating Inducer," *The 8th International Symposium on Cavitation*, edited by Ohl, C.-D., Klaseboer, E., Ohl, S. W., Gong, S. W., and Khoo, B. C., Research Publ. Services, Singapore, 2012, Paper CAV2012. doi:10.3850/978-981-07-2826-7_104

[15] Janigro, A., and Ferrini, F., "Inducer Pumps," *Recent Progress in Pump Research*, Lecture Series 61, von Kármán Inst. for Fluid Dynamics, Sint-Genesius-Rode, Belgium, 1973.

[16] Acosta, A. J., "An Experimental Study of Cavitating Inducers," *Proceedings of 2nd Symposium on Naval Hydrodynamics*, Office of Naval Research, Dept. of the Navy, Washington, D.C., 1958, pp. 533–557.

[17] Aoki, M., and Yamamoto, K., "Inlet Reverse Flow Mechanism in Axial Flow Turbomachines with Neither Stall nor Significant Radial Flow," *Journal of Turbomachinery*, Vol. 114, No. 2, April 1992, pp. 392–397. doi:10.1115/1.2929156

[18] Yokota, K., Kurahara, K., Kataoka, D., Tsujimoto, Y., and Acosta, A. J., "A Study of Swirling Backflow and Vortex Structure at the Inlet of an Inducer," *Transactions of the Japan Society of Mechanical Engineers, International Journal Series B*, Vol. 42, No. 3, 1999, pp. 451–459. doi:10.1299/kikaib.64.1667

[19] Ehrlich, D. A., and Murdock, J. W., "A Dimensionless Scaling Parameter for Thermal Effects on Cavitation in Turbopump Inducer," *Journal of Fluids Engineering*, Vol. 137, No. 4, April 2015, Paper 041103. doi:10.1115/1.4029260

[20] Ito, Y., Wakamatsu, H., and Nagasaki, T., "Numerical Simulation of Sub-Cooled Cavitating Flow by Using Bubble Size Distribution," *Journal of Thermal Science*, Vol. 12, No. 4, 2003, pp. 350–356. doi:10.1007/s11630-003-0043-7

[21] Ito, Y., Sawasaki, K., Tani, N., Nagasaki, T., and Nagashima, T., "A Blowdown Cryogenic Cavitation Tunnel and CFD Treatment for Flow Visualization around a Foil," *Journal of Thermal Science*, Vol. 14, No. 4, 2005, pp. 346–351. doi:10.1007/s11630-005-0056-5

[22] Ito, Y., Seto, K., and Nagasaki, T., "Periodical Shedding of Cloud Cavitation from a Single Hydrofoil in High-Speed Cryogenic Channel Flow," *Journal of Thermal Science*, Vol. 18, No. 1, 2009, pp. 58–64. doi:10.1007/s11630-009-0058-9

[23] Kamijo, K., Shimura, T., Hashimoto, R., Yamada, H., Nosaka, M., Suzuki, M., Watanabe, M., Watanabe, Y., Hasegawa, S., Kikuchi, M., and Sogame, E., "The Development and Study of the Turbopump System for LOX and LH2 Rocket Engine," National Aerospace Lab. TR-696, Miyagi, Japan, 1982.

[24] Yamada, H., Watanabe, M., Hasegawa, S., and Kamijo, K., "The Performance of a Cryogenic Pump for the Two-Phase Flow Condition," National Aerospace Lab. TR-870, Miyagi, Japan, 1985.

[25] Sarosdy, L. R., and Acosta, A. J., "Note on Observations of Cavitation in Different Fluids," *Journal of Basic Engineering*, Vol. 83, No. 3, Sept. 1961, pp. 399–400. doi:10.1115/1.3658979

[26] Gadd, G. E., and Grant, S., "Some Experiments on Cavities Behind Disks," *Journal of Fluid Mechanics*, Vol. 23, No. 4, 1964, pp. 645–656. doi:10.1017/S002211206500160X

[27] Yoshida, Y., Kikuta, K., Niiyama, K., and Watanabe, S., "Thermodynamic Parameter on Cavitating in Space Inducer," *Proceedings of the ASME 2012 Fluids Engineering Division Summer Meeting*, American Soc. of Mechanical Engineers Paper FEDSM2012-72212, Fairfield, NJ, 2012. doi:10.1115/FEDSM2012-72212

[28] Hinze, J. O., "Fundamentals of the Hydrodynamic Mechanism of Splitting in Dispersion Processes," *AIChE Journal*, Vol. 1, No. 3, 1955, pp. 289–295. doi:10.1002/aic.690010303

[29] Azad, M. A. K., and Syeda, S. R., "A Numerical Model for Bubble Size Distribution in Turbulent Gas-Liquid Dispersion," *IEB Journal of Chemical Engineering*, Vol. 24, No. 1, 2006, pp. 25–34.

[30] Uchiumi, M., Kamijo, K., Hirata, K., Konno, A., Hashimoto, T., and Kobayasi, S., "Improvement of Inlet Flow Characteristics of LE-7A Liquid Hydrogen Pump," *Journal of Propulsion and Power*, Vol. 19,

No. 3, 2003, pp. 356–363.
doi:10.2514/2.6139

[31] Taylor, G. I., "Stability of a Viscous Liquid Contained Between Two Rotating Cylinders," *Philosophical Transactions of the Royal Society of London, Series A: Mathematical and Physical Sciences*, Vol. 223, Feb. 1923, pp. 289–343.
doi:10.1098/rspa.1923.0013